

# Application of Chimera with Hexahedral Blocks in Solar Meshes

Simone Crippa\*

*Institut für Aerodynamik und Strömungstechnik, DLR, 38108, Braunschweig*

## Abstract

The Chimera methodology of the DLR TAU solver is evaluated in this study for enhancing unstructured Solar grids. The discretization improvements using hexahedral blocks are demonstrated on a five-block grid of the NASA CRM and a two-block grid for the NASA Trapezoidal Wing. A vast potential for discretization improvements of Solar grids is found, but further assessments need to take into account the computational overhead still required by this non-native approach in TAU.

## 1 Introduction

The capabilities of the DLR TAU solver for the computation on overset — or Chimera — grids are evaluated in this study. The Chimera technology is used in the scope of this study, as a way to enhance the default unstructured grids generated with Solar. Solar is a collaborative development of BAE Systems ATC, BAE Air Systems, Airbus, QinetiQ and ARA and is a major corporate grid generation package at Airbus. The methodologies implemented in the grid generation software Solar are aimed at minimizing user input, and thus result in a high level of automation. The employed advancing-layer grid generation method results in a global O-type grid topology around solid surfaces. This type of near-wall discretization has some pitfalls, as in critical areas the local flow topology may not be resolved by an appropriate grid topology. The boundary layer in concave surface junctions or shear layers downstream of thin trailing edges are just two examples, where the flow topology can not be matched by an O-type grid topology. The penalty of global O-type grid topology on solution accuracy is not inherently coupled to the CFD solution strategy. Both unstructured and structured solvers can deliver poor results in certain aspects when dealing with global O-type topologies. Recent efforts[1] have tried to improve the advancing-layer methodology for concave junction discretization, while still delivering a point-matching grid.

For this study, two Solar grids for two different configurations are enhanced by the addition of hexahedral grid blocks. The two configurations, for which extensive experience was gathered in past studies, are enhanced in the concave junctions between lifting surface(s) and body.

One of the evaluated configuration is the NASA Common Research Model[2] (CRM), in the reduced configuration of wing/body/horizontal-tail, also used for the fourth Drag Prediction Workshop (DPW-4)[3]. The design point of the CRM is at a cruise Mach number of  $M =$

---

\*Research Associate, C<sup>2</sup>A<sup>2</sup>S<sup>2</sup>E branch

0.85, lift coefficient  $C_l = 0.5$  and Reynolds number based on the mean aerodynamic chord of  $Re = 40 \cdot 10^6$  at a cruise altitude of 37000ft. As for DPW-4, a reduced Reynolds number of  $Re = 5 \cdot 10^6$  was chosen for this study, which matches the conditions of two wind-tunnel campaigns.

The second configuration is the three-element, high-lift NASA Trapezoidal Wing, that was the focus of the efforts during the first AIAA High Lift Prediction Workshop (HiLiftPW-1)[4]. The full configuration is evaluated, featuring also the flap and slat holding brackets.

## 2 DLR TAU CFD Solver

The unstructured flow solver TAU[5] solves the Reynolds-averaged Navier-Stokes equations with a second-order finite-volume discretization. The capability of the unstructured flow solver TAU[5] to compute on overset grids is a relatively recent development[6]. The overset grid capability was mainly implemented for being able to add single components to a given grid, to perform relatively large movements of surfaces or to perform multi-body simulations. Due to the inherent flexibility of the unstructured grid generation process, the need for a comprehensive overset grid capability was not highly prioritized. This led to the implementation of only basic functionalities.

- The hole-cutting operation for determining the blanking of grid points is performed during the initialization of the solver, by using simple hole-cutting geometries provided in the TAU NetCDF format.
- The wall distance projection as implemented previously in the DLR FLOWer solver[7], was also implemented in TAU with the addition of an unstructured point projection method.
- The integration of forces and moments on solid surfaces is at this time only possible with a development version of TAU in serial execution mode.

## 3 Chimera Grids

The Chimera grids evaluated in this study are each composed of a background Solar grid, discretizing the complete flow-field, with the addition of one, or more hexahedral component grids. Each of the component grids are paired to hole-cutting geometries, which are used to blank the points of the background Solar grid, as to guarantee a discretization of some regions by the component grids alone. The data obtained on the background grid alone, can thus be compared to the Chimera grid results. The chosen incremental discretization approach highlights the solution improvements given solely by the additional grid blocks.

### 3.1 Background Solar Grids

The background grids were chosen as the medium resolution members of the three-level grid families generated for DPW-4 or HiLiftPW-1.

The background Solar grid for the CRM was generated by using so-called philosophy files for high-speed configurations, yielding the baseline, medium grid resolution with 11.7 million points. See Crippa[8] for a detailed description of the baseline Solar grid.

The grid generation for HiLiftPW-1 was more intricate, as no philosophy files or best-practice guidelines were available for high-lift configurations and overall experience to generate Solar grids on these configurations was very limited. The final grid for the Trapezoidal Wing with brackets features 39.7 million points; for further reference see Crippa et al[9].

### 3.2 Additional Hexahedral Grid Blocks

A C-H-type topology is selected for the collar grids to resolve the junctions. The H-topology resolves the boundary layers of the lifting surfaces and the bodies, whereas the C-topology is wrapped around the leading edge and resolves the shear layers downstream of the leading edges. A C-H-type topology is also used for the wake-resolving grids of the CRM configuration, where the curved, C-type topology resolves the blunt wing/HTP trailing edges.

The additional hexahedral grid blocks for the CRM were generated with ANSYS ICEM CFD or DLR MegaCads. As the additional grid blocks were generated after the background Solar grid, the discretization at the boundaries of the hexahedral blocks had to be adapted to the given discretization of the Solar grids. This step is important, as similar element sizes in the overlap region are useful to minimize interpolation errors. The component grids resolving the wing-fuselage junction, the wing trailing edge/wake, and the HTP trailing edge/wake were generated with ANSYS ICEM CFD and feature respectively 5.25, 2.39, and 0.46 million grid points. The component grid resolving the HTP-fuselage junction was generated with the DLR MegaCads grid generator and features 0.64 million grid points.

The collar grid for the Trapezoidal Wing was extracted from a fully-hexahedral grid provided by a participant[10] of HiLiftPW-1. The originally structured grid generated at JAXA with Gridgen is the medium-level member of the grid family and features 36.7 million points. The extracted block used to enhance the Solar grid features 5.01 million points.

### 3.3 Five-Block CRM Grid

The assembly of the Solar background grid and the four component hexahedral blocks for the CRM was performed with `setup_taugrid`. The resulting Chimera grid, which will be referred to as “SolarChimera5Block” hereafter, presented in figure 1, features 20.42 million grid points. Due to blanking by the hole-cutting geometries, only 17.22 million grid points are relevant to the computation. The interpolation of data between grid blocks is performed in 1.26 million grid points in the overlap regions.

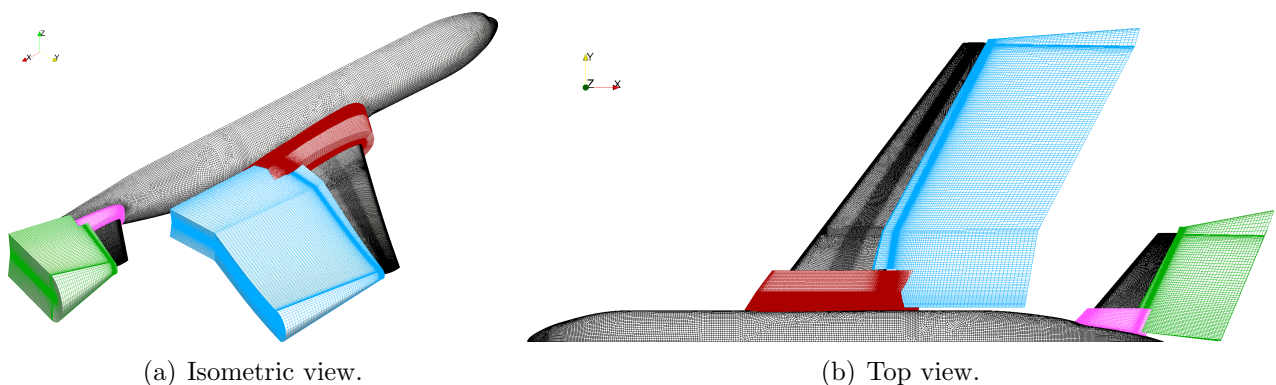


Figure 1: Five-block CRM Chimera grid.

With the chosen Chimera block structure, three blocks at the root and trailing edge of the lifting surfaces can potentially overlap. An overlap on the solid walls was avoided on purpose. With the employed TAU release, the mismatch of the geometries in the overlap region is not taken correctly into account if wall projection needs to be applied to more than one block. The overlap of multiple blocks is not problematic in the field, or when no wall projection is required. To visualize the three-block overlap in the field, a  $z$ -constant cut is shown in figure 2, along with the corresponding surface mesh of the three grid blocks. It is possible to recognize the overlap of the Solar grid with either the collar grid or the wing wake grid on the surface, whereas in the field the three blocks overlap each other.

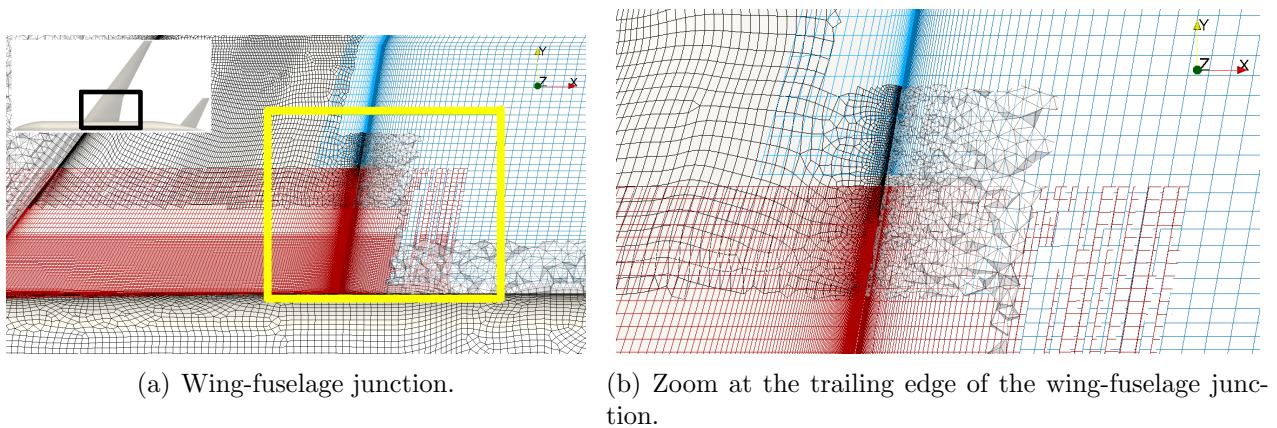


Figure 2: Top view of field cut ( $z = 200''$ ) through the five-block CRM Chimera grid; Solar grid with black edges — partly translucent in the field — wing-fuselage collar grid in red and wing wake grid in blue.

### 3.4 Two-Block Trap-Wing Grid

The combined Solar and Gridgen-extracted grid for the Trapezoidal Wing configuration features 44.72 million grid points, see figure 3. Subtracting blanked points from the Chimera grid results in 41.95 million points, with an additional 0.32 million points in the interpolation region.

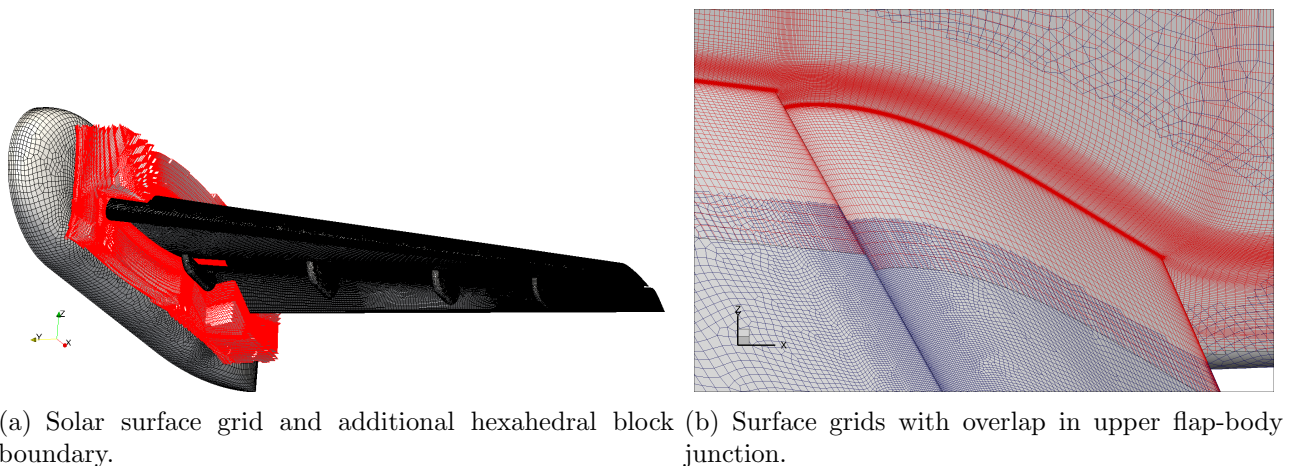


Figure 3: Two-block Trapezoidal Wing Chimera grid.

### 3.5 Integration of Forces and Moments on Solid Walls

When two or more grid blocks overlap on a viscous surface, a special treatment is required to determine the integral forces and moments of the complete body. A development version of TAU features the same method as in the DLR FLOWer solver implemented by Schwarz[7]. The gap between fully-blanked surface grids is triangulated (zipped) in order to gain a closed wall surface. The wall normals of the overset grids at the borders of the gap are then corrected by taking the triangulated zipper grid into account. Due to the development status of this method, the correction of the angle of attack for the target-lift-coefficient computations was performed manually. The fringes of the overlapping grid blocks, which are connected by the zipper mesh, are visualized for the CRM in figure 4.

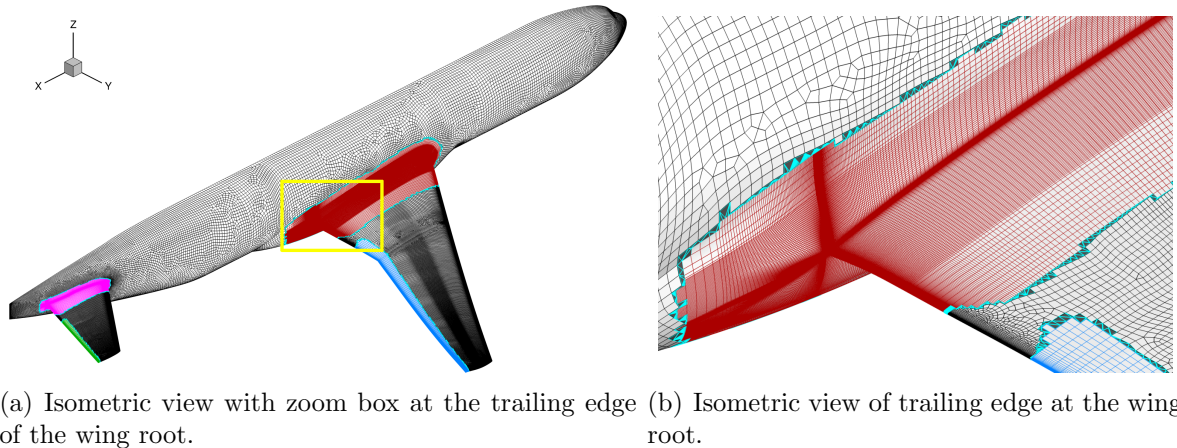


Figure 4: Closed wall surface for forces and moments integration; zipper mesh in dark gray with cyan edges.

## 4 Results and Discussion

All the computations in this study were performed with the DLR TAU release 2011.1.0 and the Spalart-Allmaras (SAO) turbulence model. The solution procedure consisted in a short, three-level full multigrid initialization with an upwind scheme for the inviscid fluxes, then a switch to a three-level multigrid cycle with central scheme and finally a switch to single-grid. The numerical settings for the employed central scheme with scalar dissipation are  $k_2 = 0.25$  and  $1/k_4 = 64$ .

### 4.1 CRM - Target Lift Coefficient of 0.5

For the target lift coefficient ( $C_l = 0.5$ ) computations, the comparison between the grids in terms of integrated forces and moments is summarized in table 1.

Table 1: Forces and moment coefficients for target-lift-coefficient  $C_l = 0.5$ .

Grid	Angle of attack	$C_l$	$C_d$	$C_{my}$
Solar	2.29948°	0.5000	0.02718	-0.03996
SolarChimera5Block	2.36387°	0.5000	0.02743	-0.03843

To achieve the same lift coefficient on both grids, the angle of attack for the Solar5BlockChimera computation has to be increased by approx.  $0.06^\circ$ . Due to the increase of angle of attack for achieving the same lift coefficient, it is not trivial to separate the effects of an improved field discretization on the forces and moments, from the indirect effects of for instance a shift in shock positions.

At a fixed lift coefficient, the difference between the two grids leads to a minor increase of drag coefficient ( $C_d$ ) by 2.5 drag counts (dc)<sup>1</sup>. A slightly higher effect is found for the pitching moment coefficient ( $C_{my}$ ). An analysis of the differences between the results on the two sets of grids, reveals that a minute wing-body separation is resolved in the Chimera grid, which is not resolved in the Solar grid alone. This separation does neither affect shock position nor pressure coefficient in a dramatic way[8]. An other minute, topologically similar, junction-flow separation is also found on the upper side of the HTP-fuselage. The effect of the junction separations is analyzed in detail for a fixed angle of attack.

## 4.2 CRM - Off-Design Condition at $4^\circ$ Angle of Attack

At this off-design condition, both the comparison of integrated forces and moment coefficients, and the discretization deficiencies of the plain Solar grid are more clear.

The integrated forces and moments for the fixed angle of attack of  $4^\circ$  are summarized in table 2. The difference in lift coefficient of only 0.05 is nearly negligible, relative to the decrease

Table 2: Forces and moment coefficients for angle of attack of  $4^\circ$ .

Grid	Angle of attack	$C_l$	$C_d$	$C_{my}$
Solar	$4^\circ$	0.6887	0.05208	-0.0590
SolarChimera5Block	$4^\circ$	0.6354	0.04657	-0.1791

of drag and pitching moment coefficients by 55 dc and 0.12 respectively. The reason for these differences are again found in the resolution of the wing/HTP-fuselage separation bubbles, that expand substantially at this incidence.

On the Solar grid, a separation in the wing-fuselage junction is still not found at this incidence, see figure 5(a). On the Chimera grid, the minute trailing-edge-confined separation

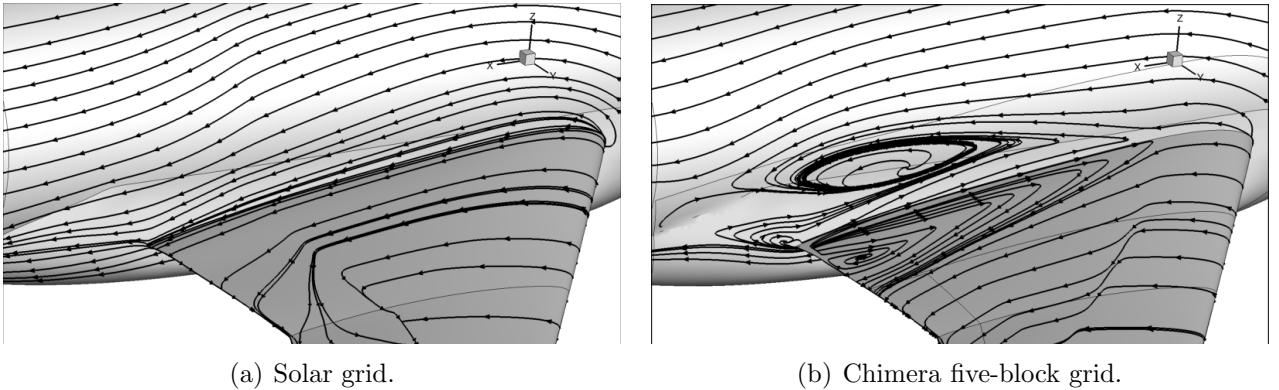


Figure 5: Skin friction lines on the CRM wing and fuselage at the incidence of  $4^\circ$ .

<sup>1</sup>one drag count is a single unit of drag coefficient, i.e. 1 drag count is equal to a  $C_d$  of  $1 \cdot 10^{-4}$ .

bubble at the  $C_l = 0.5$  condition, now expands and starts at  $x/c_{root} \approx 0.3$ . The flow-field of the inner wing section is dominated by the junction separation, see figure 5(b), with a substantial effect on the shock strength and position.

In contrast to the situation at  $C_l = 0.5$ , where the separation is confined to the junction and has no major effect on the wing, at this off-design incidence, the under-resolved junction of the Solar grid leads to a quantitatively and qualitatively unsatisfying result. The direct comparisons between the Chimera grid and the plain background Solar grid, reveal its discretization deficiencies. The improvement of the solution through the addition of the hexahedral blocks is remarkable, in terms of forces and moment coefficients at target-lift coefficient of  $C_l = 0.5$  and at the incidence of  $4^\circ$ .

The eddy viscosity development in the wake of the lifting surfaces is obviously better discretized by the flow-aligned, highly stretched hexahedra of the Chimera grid, as compared to the isotropic, larger tetrahedra of the Solar grid. The difference is visualized in figure 6 for a plane in the wake of the wing. In contrast to the Solar solution, the wake of the large wing-fuselage

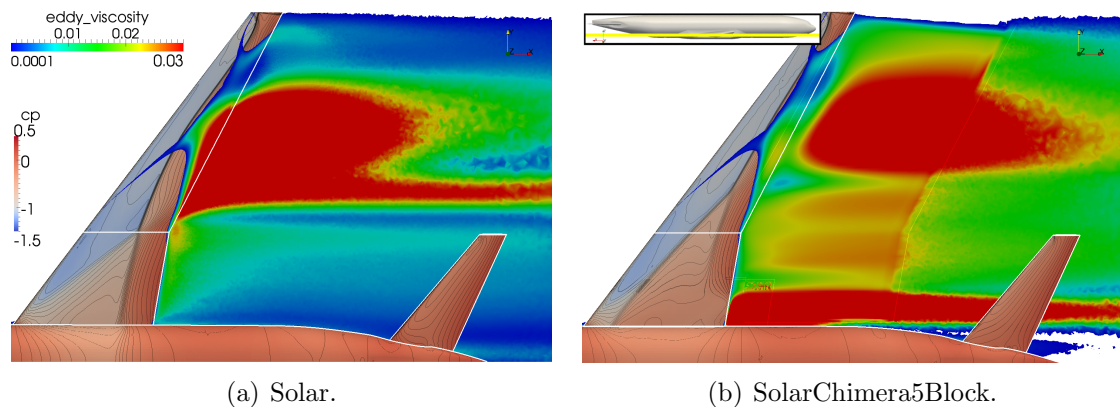


Figure 6: Top view on the CRM surface colored by pressure coefficient ( $cp$ ), with a wing-wake plane aligned with the inner wing trailing edge colored by eddy viscosity (clipped at 0.0001).

junction separation extends beyond the HTP in the SolarChimera5Block solution. The indirect effect of the wing-fuselage separation on the wing shock strength and position influences the complete wing from root to tip. This results in large differences of eddy viscosity already just aft of the trailing edge. Notice that in figure 6(b), it is also possible to recognize the resolution jump from the hexahedra wing-wake block to the Solar background grid, whereafter eddy viscosity is dissipated quickly due to the transition to relatively large tetrahedral elements.

A  $y$ -constant cut plane inboard of the kink further highlights the improved resolution of the wing wake hexahedra block, see figures 7(a) and 7(b).

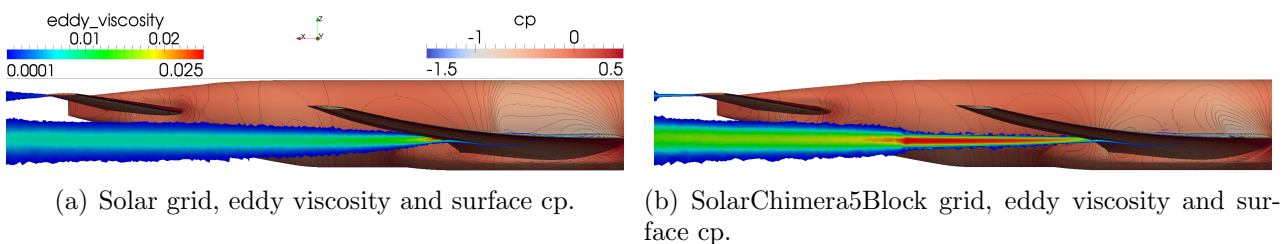


Figure 7: Side view on the CRM surface colored by pressure coefficient ( $cp$ ), with a  $y = 399''$  plane colored by eddy viscosity (clipped at 0.0001)

Further insight in the difference of the flow-field being resolved by the two grids is gained by visualizing x-constant cut planes in the wake of the wing, see figure 8.

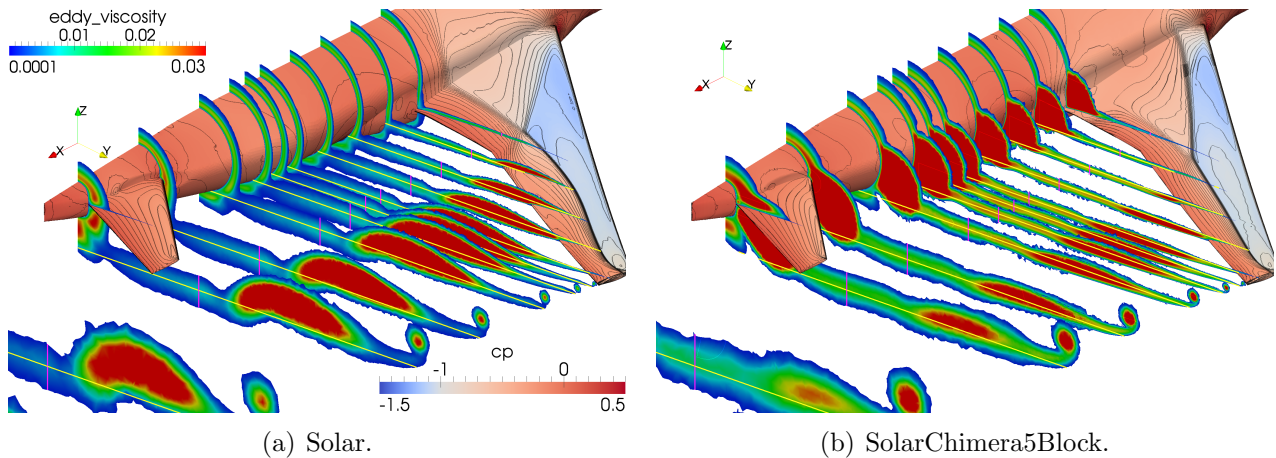


Figure 8: Isometric view on the CRM surface colored by pressure coefficient (cp), with x-constant planes colored by eddy viscosity (clipped at 0.0001). The cuts shown in figure 6 and figure 7 are traced in yellow or pink.

The downstream development of the wing-body junction separation has a major influence on the HTP effectiveness. Wingtip vortex and shock-induced separation on the outboard wing are also resolved differently in the two grids.

### 4.3 Trapezoidal Wing at 13° Angle of Attack

The improved junction discretization given by the Chimera grid on the Trapezoidal Wing, allows a qualitative improvement of several flow-features. The slat-body and main-body horseshoe vortices development over the chord is captured more accurately. The interaction of the shear layer downstream of the slat trailing edge with the boundary layers of body, main element and flap is improved. The effect of the improved resolution of these flow features on the overall forces and moments is measurable, but negligible. The flap-body separation is qualitatively similar in the results of both grids, see figure 9.

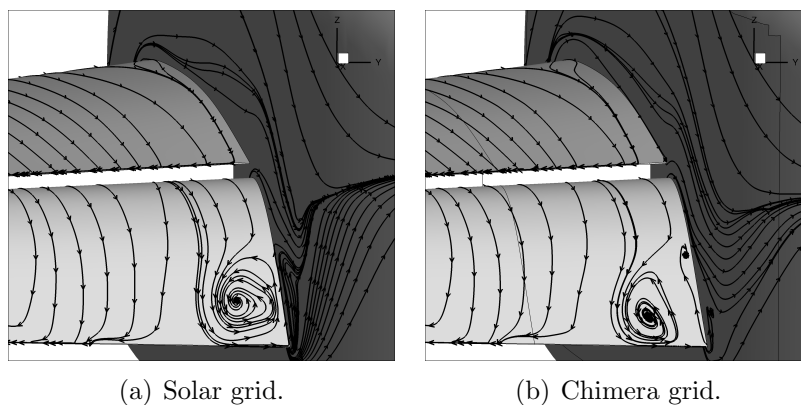


Figure 9: Rear view on the skin friction lines of the upper body junctions with the flap and main wing elements.

Although the discretization improvement was targeted at the flap-body junction, some differences in the results are found upstream of the flap. The comparison in the one-quarter cut plane presented in figure 10 reveals that the horse-shoe vortex originating from the slat-body is located in the same position above the body pod, but the strength is different. Under the slat-body horse-shoe vortex, in the junction between main element and body pod, the main-body horse-shoe vortex develops in a substantially different way. Regardless of the grid, the main-body vortex interacts with the shear layer from the slat trailing edge in a complex manner. The vortex core seems to be resolved similarly in the two grids, but the secondary flow effects are different. A slight vortex core dilation is found in the Solar grid, compared to the Chimera grid result.

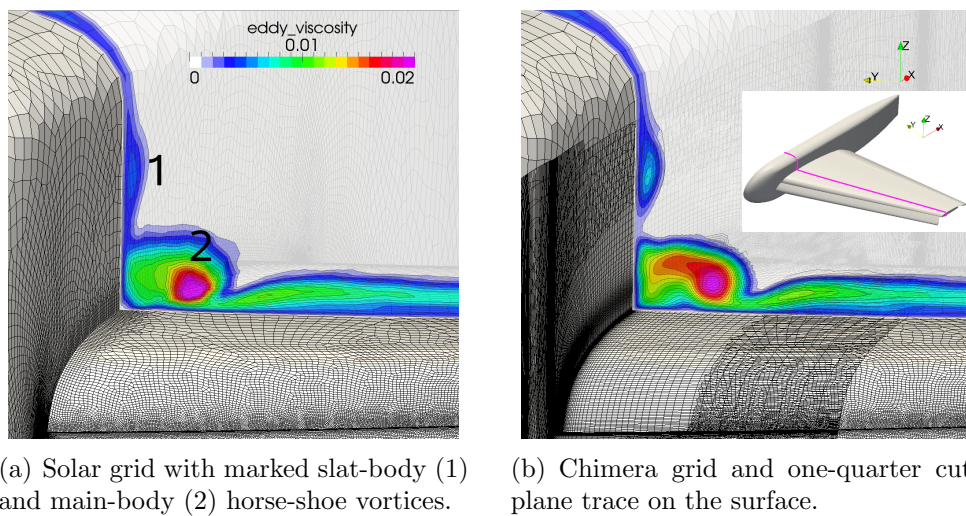


Figure 10: Front view on the one-quarter cut plane with surface grids.

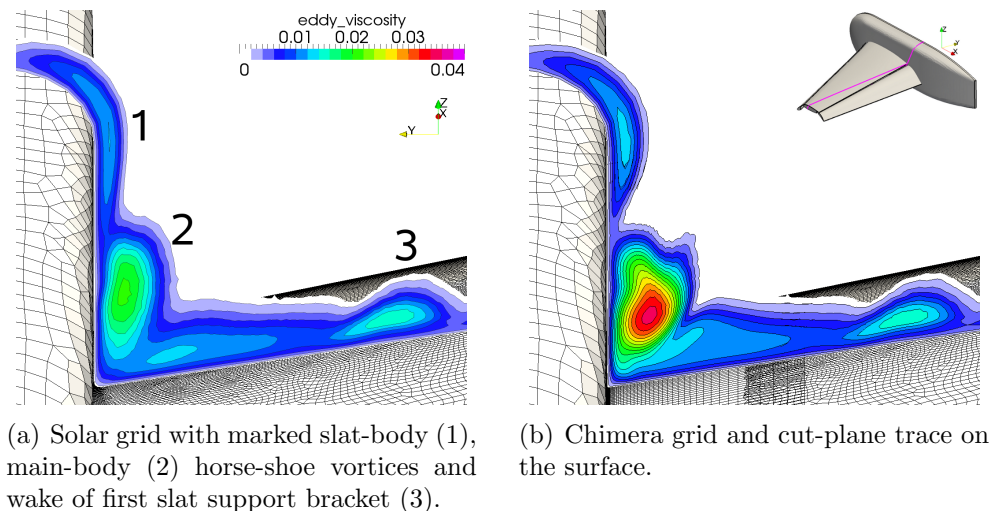
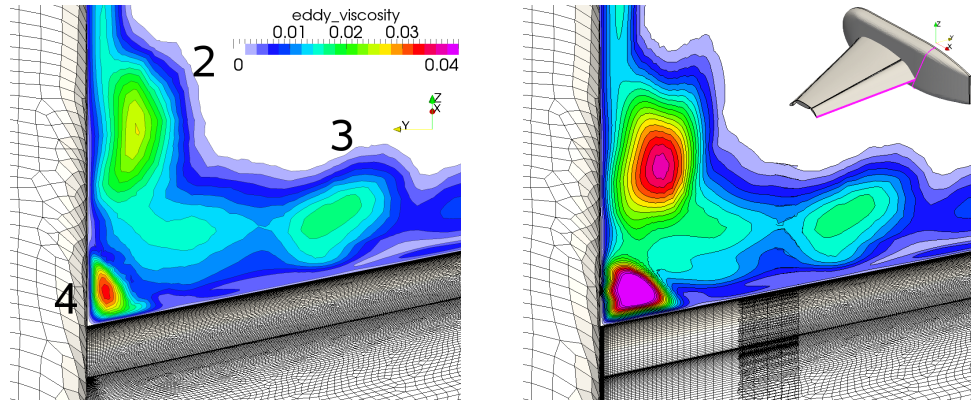


Figure 11: Front view on a cut plane near the main element trailing edge with surface grids.

Figure 11 presents field cut planes located at the main wing trailing edge. At the begin of the flap-body junction, the resolution deficiency of the upstream horse-shoe vortices in the Solar grid is apparent. Both horse-shoe vortices are more compact in the Chimera grid and

show a higher strength. The wake of the first slat support bracket, being resolved only in the Solar grid block, shows consistently the same pattern in both grids.

Further downstream in the flap-body junction, the resolution differences of the upstream flow structures lead to a further major deviation between the two grids. Figure 12 presents field cut planes located at the flap trailing edge. In the Chimera grid, the main-body horse-shoe



(a) Solar grid with marked main-body (2) horse-shoe vortex, wake of first slat support bracket (3), and flap-body junction separation (4).

(b) Chimera grid and cut-plane trace on the surface.

Figure 12: Front view on a flap trailing-edge-normal cut plane with surface grids.

vortex is stronger and located closer to the junction. The flap-body separation bubble is present in both solutions, but the topology and interaction with the main-body horse-shoe vortex is clearly different.

## 5 Conclusions

Discretization improvements of baseline Solar grids with hexahedral blocks, using the Chimera capabilities of the DLR TAU code were demonstrated. A five-block Chimera grid of the NASA CRM and a two-block grid for the NASA Trapezoidal Wing were assembled and the individual discretization improvements assessed.

In the case of the CRM configuration, the effort to generate each separate hexahedra grid block is relatively small. On the other hand, a substantial part of the overall effort is then necessary to perform two additional, manual and thus time-consuming steps.

1. The outer boundaries of the wake-resolving blocks need to be matched to the given Solar grid.
2. Given a set of overlapping grids, the hole-cutting geometries must be tweaked to allow for an appropriate overlap between the blocks.

The first obstacle to a swift Chimera grid generation process can be overcome by including the need for a finer wake field discretization at the first stage, i.e. during the initial Solar grid generation by using Chimera-adapted philosophy files. If the grid blocks feature similar element sizes in the overlap, the second problem of finding appropriate hole-cutting geometries, might then be solved more easily. An alternative, automatic hole-cutting procedure alone, without

addressing the first point, might ease the effort required for the second step, but a sub-optimal overlap might still lead to undersized, sub-optimal blanking regions.

The blanked-out grid points of the CRM Chimera grid are 15.7% of the total grid points, whereas for the Trapezoidal Wing grid, this value is 6.2%. The higher figure for the CRM Chimera grid is due to relatively more points being blanked out from the background Solar grid than in the case of the Trapezoidal Wing Chimera grid. In the case of the Trapezoidal Wing configuration, using two given grid blocks leaves only the user-defined hole-cutting geometry to achieve an appropriate overlap between the blocks. As the geometry is relatively complex, also due to the slat and flap supporting brackets on the pressure side, regardless of the manual effort the hole-cutting geometry is relatively small. This leads to a relatively large interpolation overlap, with largely different element volumes in the field. The grid points out of the total used for data interpolation between the blocks amount to 6.2% for the CRM and 7% for the Trapezoidal Wing. These values are similar, although the CRM Chimera grid features more overlap regions than the Trapezoidal Wing, due to the manual matching of the additional grid blocks performed for the CRM configuration.

The vast potential for discretization improvements of Solar grids is documented in this study. The feasibility of using Chimera for this purpose was proven, but further assessments need to take into account the computational overhead still required by this non-native approach in TAU.

## References

- [1] Ito, Y., Murayama, M., Yamamoto, K., Shih, A. M., and Soni, B. K., “Efficient Hybrid Surface and Volume Mesh Generation for Viscous Flow Simulations,” Paper 2011-3539, AIAA, Honolulu, Hawaii, June 2011, 20th AIAA Computational Fluid Dynamics Conference.
- [2] Vassberg, J., DeHaan, M., Rivers, S., and Wahls, R., “Development of a Common Research Model for Applied CFD Validation Studies,” Paper 2008-6919, AIAA, June 2008.
- [3] Vassberg, J. C., Tinoco, E. N., Mani, M., Rider, B., Zickuhr, T., Levy, D. W., Brodersen, O., Eisfeld, B., Crippa, S., Wahls, R. A., Morrison, J. H., Mavriplis, D. J., and Murayama, M., “Summary of the Fourth AIAA CFD Drag Prediction Workshop,” *28th AIAA Applied Aerodynamics Conference*, June 2010, AIAA 2010-4547.
- [4] Slotnick, J. P., Hannon, J. A., and Chaffin, M., “Overview of the 1st AIAA CFD High Lift Prediction Workshop,” Paper 2011-0862, AIAA, Orlando, FL, January 2011.
- [5] Schwamborn, D., Gerhold, T., and Heinrich, R., “The DLR TAU-Code: Recent Applications in Research and Industry,” *In Proceedings of the European Conference on Computational Fluid Dynamics, ECCOMAS CFD 2006*, edited by P. Wesseling, E. Oñate, and J. Périaux, The Netherlands, 2006.
- [6] Madrane, A., Raichle, A., and Stürmer, A., “Parallel Implementation of a Dynamic Overset Unstructured Grid Approach,” *Proceedings of the 4<sup>th</sup> European Congress on Computational Methods in Applied Sciences and Engineering, ECCOMAS 2004, Jyväskylä, Finland, July 24-28, 2004*, edited by P. Neittaanmäki, T. Rossi, S. Korotov, E. O. nate, J. Périaux, and D. Knörzer, University of Jyväskylä, Jyväskylä, 2004, ISBN 951-39-1869-6.

- [7] Schwarz, T., “The overlapping grid technique for the time accurate simulation of rotorcraft flows,” *Proceedings of the 31st European Rotorcraft Forum*, Confederation of European Aerospace Societies, CEAS, Florence, Italy, September 2005.
- [8] Crippa, S., “Application of Novel Hybrid Mesh Generation Methodologies for Improved Unstructured CFD Simulations,” Paper 2010-4672, AIAA, June 2010.
- [9] Crippa, S., Melber-Wilkending, S., and Rudnik, R., “DLR Contribution to the First High Lift Prediction Workshop,” *Proceedings of the 49th AIAA Aerospace Sciences Meeting*, AIAA, Orlando, FL, January 2011, AIAA 2011-0938.
- [10] Murayama, M., Yamamoto, K., and Kobayashi, K., “Validation of Computations Around High-Lift Configurations by Structured- and Unstructured-Mesh,” *Journal of Aircraft*, Vol. 43, No. 2, 2006, pp. 395–406, doi: 10.2514/1.15445.